Using Bulk Heterojunctions and Selective Electron Trapping to Enhance the Responsivity of Perovskite–Graphene Photodetectors

Liang Qin, Liping Wu, Bhupal Kattel, Chunhai Li, Yong Zhang, Yanbing Hou, Judy Wu, and Wai-Lun Chan**

Graphene field effect transistor sensitized by a layer of semiconductor (sensitizer/GFET) is a device structure that is investigated extensively for ultrasensitive photodetection. Among others, organometallic perovskite semiconductor sensitizer has the advantages of long carrier lifetime and solution processable. A further step to improve the responsivity is to design a structure that can promote electron–hole separation and selective carrier trapping in the sensitizer. Here, the use of a hybrid perovskite–organic bulk heterojunction (BHJ) as the light sensitizer to achieve this goal is demonstrated. Our spectroscopy and device measurements show that the $CH_3NH_3PbI_3$–PCBM BHJ/GFET device has improved charge separation yield and carrier lifetime as compared to a reference device with a $CH_3NH_3PbI_3$ sensitizer only. The key to these enhancement is the presence of [6,6]-phenyl-C_{61}-butyric acid methyl ester (PCBM), which acts as charge separation and electron trapping sites, resulting in a 30-fold increase in the photoresponsivity. This work shows that the use of a small amount of electron or hole acceptors in the sensitizer layer can be an effective strategy for improving and tuning the photoresponsivity of sensitizer/GFET photodetectors.

1. Introduction

Because of its high charge carrier mobility, graphene has been an attractive material for various optoelectronic applications.[1–3] In particular, its electronic properties can be sensitive to charge doping induced by the substrate, electrical gating, and optical excitation.[4–7] When combining a graphene field effect transistor (GFET) with "sensitizers" that can transduce signals to charges in graphene, this sensitizer/GFET nanohybrid device has the superior light absorption and charge mobility of its constituent components for high-sensitivity photodetection and sensing.[8,9] Different photosensitizers, such as inorganic quantum dots,[9–11] plasmonic nanoparticles,[12] organic semiconductors,[13,14] 2D layered crystals,[15,16] and hybrid organometallic perovskites,[17,18] are used to sensitize the graphene channel. In these sensitizer/GFET devices, light is absorbed by the sensitizer to generate electron–hole pairs. Depending on the interfacial band alignment, either electrons or holes are preferentially transferred to graphene. The remaining carriers in the sensitizer produces a photogating effect in graphene, which is then illustrated as a change in the conductivity of the graphene channel as the photoresponse. A distinct advantage of this detection mechanism compared to those based on photovoltaic effects is the much higher photoresponsivity enabled by the high carrier mobility of graphene.[8]

The change in the graphene's conductivity depends on the net amount of electrons or holes remained in the sensitizer. Hence, any mechanism that selectively traps one type of carriers in the sensitizer while injects the other type of carriers into graphene can enhance the photoresponse. Organometallic halide perovskites have been chosen as the light sensitizer in GFET devices[17–23] because of its long carrier lifetime and diffusion length, and its outstanding performance in photovoltaic application.[24–26] However, most of the perovskite photodetectors investigated so far do not have a mechanism to promote electron–hole separation and selective charge trapping. In these devices, the asymmetry between electron and hole transfer to graphene is induced by the intrinsic band bending at the semiconductor–graphene interface,[9] which is rather difficult to control. The

L. Qin, C. Li, Prof. Y. Hou
Key Laboratory of Luminescence and Optical Information
Ministry of Education
Beijing JiaoTong University
Beijing 100044, China

L. Qin, L. Wu, B. Kattel, Y. Zhang, Prof. J. Wu, Prof. W.-L. Chan
Department of Physics and Astronomy
University of Kansas
Lawrence KS 66045, USA
E-mail: jwu@ku.edu; wlchan@ku.edu

L. Wu
Department of Materials Science and Engineering
Shanghai Jiao Tong University
Shanghai 200240, China

Y. Zhang
School of Microelectronics and State Key Laboratory
for Mechanical Behavior of Materials
Xi'an Jiaotong University
Xi'an 710049, China

The ORCID identification number(s) for the author(s) of this article can be found under https://doi.org/10.1002/adfm.201704173.

DOI: 10.1002/adfm.201704173

energy barrier created by the band bending would be small for some interfaces. To further complicate the interfacial design, the band alignment can also depend on the crystal orientation of the semiconductor with respect to graphene, although this factor is usually neglected. Other strategies have been employed to selectively block the charge transfer to graphene. For example, it has been demonstrated that a poly(3-hexylthiophene) (P3HT) layer underneath the perovskite layer can be used to block the electron transfer to graphene.[23] However, processes such as electron–hole recombination within the sensitizer layer prior to carrier extraction at the sensitizer/graphene interface would still limit the photoresponse. Therefore, to optimize the light sensitivity, several key points should be taken into consideration: (i) to promote effective electron–hole separation in the photoactive layer; (ii) to selectively inject one type of the carriers into graphene; and (iii) to maximize the trapping time (i.e., the lifetime) of the other type of carriers within the photoactive layer.

In this work, a bulk heterojunction (BHJ) film is used as the sensitizer to fulfill the above requirements. This BHJ consists of $CH_3NH_3PbI_3$ organometallic halide perovskite and [6,6]-phenyl-C_{61}-butyric acid methyl ester (PCBM). BHJ has long been used in organic photovoltaics to enhance the charge carrier separation efficiency.[27,28] Recently, it has been shown that the $CH_3NH_3PbI_3$–PCBM BHJ can enhance the perovskite solar cell efficiency and stability.[29,30] In the $CH_3NH_3PbI_3$–PCBM BHJ structure, the PCBM with a low concentration are dispersed throughout the perovskite film.[29,31] The PCBM provide electron accepting sites which selectively extract electrons from the perovskite. Hence, it promotes electron–hole separation. The hole, which is known to have a long diffusion length as compared to the electron in $CH_3NH_3PbI_3$,[32] can transport effectively through the continuous perovskite matrix to reach the graphene layer. Moreover, the PCBM can effectively trap the electron. This in turn enhances the electron lifetime and the photoresponse.

To elucidate that the above scenario occurs in our perovskite–PCBM BHJ/graphene detector, reference devices without PCBM were studied in parallel in this work. Photoluminescence (PL) quenching measurement shows that the BHJ separates electrons and holes effectively and avoids carrier recombination within the BHJ layer. Ultrafast time-resolved electrical measurement demonstrates that the electron lifetime in the BHJ/graphene device is about 4–5 orders of magnitude longer than that in the perovskite/graphene device. The long electron lifetime results in a 30-fold increase in the photoresponsivity compared to the perovskite–graphene photodetector. For our perovskite–1% PCBM photodetectors, even with a rather large millimeter channel size, the photoresponsivity can already reach $\approx 10^6$ A W^{-1}. The same design strategy can be easily applied to other semiconductor–GFET photodetectors by importing a low concentration of electron acceptors (or hole acceptors) to the sensitizer material. This allows us to control the magnitude and the polarity of the photoresponse by varying the dopant type and concentration.

2. Results and Discussion

A one-step antisolvent method is used to prepare the perovskite–PCBM BHJ films on monolayer graphene.[31,33] Prior to deposition, the graphene channel (with channel length/width = 1/1 or 0.3/2 mm) and source–drain electrodes are patterned onto the substrate as described in the Experimental Section. Three different PCBM concentrations, with weight ratios of 0% (no PCBM), 0.1%, and 1%, are used in our experiment. Our BHJ film preparation procedures are similar to those used in published works,[31,33] and the details can be found in the Experimental Section. The as-prepared perovskite–BHJ films on graphene are characterized by X-ray diffraction (XRD) and scanning electron microscopy (SEM). The XRD patterns are shown in the Supporting Information (Figure S1, Supporting Information). The perovskite BHJ films and the perovskite film without PCBM have similar film textures, as shown by the similar intensity ratios between different diffraction peaks. Hence, the addition of PCBM does not significantly alter the grain orientation. Intense $CH_3NH_3PbI_3$ (110) and (220) peaks in the XRD patterns reveal a good crystallinity of the perovskite grains.[34] The surface morphology and the film thickness are measured by SEM and the images are shown in the Supporting Information (Figure S2, Supporting Information). The film thicknesses for all perovskite–PCBM samples of PCBM concentrations of 0%, 0.1%, and 1% are around 370–400 nm. The former two films have a similar columnar grain structure. In the 1% PCBM concentration film, additional grain boundaries parallel to the substrate can be found, which can be caused by the additional PCBM acting as grain nucleation sites.

Figure 1a shows the UV–vis absorption spectra of the perovskite–PCBM films with different PCBM concentrations. A typical $CH_3NH_3PbI_3$ absorption edge around 786 nm can be found in all spectra. In addition, all three samples have a similar absorption cross-section, which is consistent to the similar film thickness found in our SEM images. PCBM has a weak and broad absorption peak around 500 nm, and a stronger absorption peak around 350 nm.[35] However, in our samples, the shape of the spectra is similar for all samples. Hence, the PCBM does not contribute significantly to the optical absorption, which is expected from the low PCBM concentrations in samples studied in this work.

Despite the similarity in the optical absorption spectra, the PL peak at 776 nm for $CH_3NH_3PbI_3$ have considerably different intensities for the samples with different PCBM concentrations as shown in Figure 1b. By normalizing the PL spectra to the PL peak height (Figure S3, Supporting Information), we find that all the spectra have a similar spectral line shape and peak position. This indicates that the PCBM does not change the origin of the optical transition. However, the PL intensities for these samples are very different. The PL intensities for the 0.1% and 1% PCBM BHJ films are only ≈33% and ≈8% of that of the perovskite-only film. The significant PL intensity quenching by an order of magnitude after the PCBM addition indicates that the PCBM induces a nonradiative kinetic process that out-competes the radiative recombination in $CH_3NH_3PbI_3$. PCBM has been used as an electron acceptor in perovskite solar cells.[29] Optically excited electrons in perovskite can effectively transfer to the PCBM while holes remain in the perovskite grains. The spatial separation of electrons and holes prohibits radiative recombination. The significantly reduced PL intensity shows that the perovskite–PCBM BHJ structure is very effective in

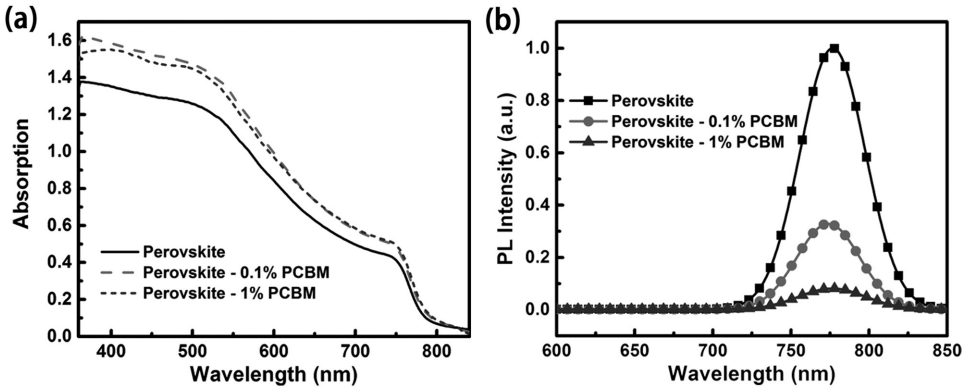

Figure 1. a) The UV–vis absorption spectra and b) PL spectra of the perovskite–PCBM BHJ films on graphene with different PCBM concentrations: 0%, 0.1%, and 1%.

separating the electrons and holes, which reduces the loss due to radiative recombination.

Figure 2a is a schematic for the structure of our BHJ–graphene photodetectors. Optical excitation creates electrons and holes in the perovskite. The PL quenching measurement demonstrates that the BHJ separates electrons and holes, with the electrons transfer to the PCBM. If the holes can transfer effectively into graphene, a net amount of negative charges will build up in the BHJ layer. This will induces hole doping in graphene, which lowers the E_f of graphene and changes the graphene conductivity. The energy level diagram of our material system and the electronic processes described above are illustrated in Figure 2b.

To demonstrate that the shift in the E_f is originated from photoinduced doping, the source–drain current of the photodetector is measured as a function of the back gate voltage (V_G) applied to the GFET. The results for the perovskite-only and the perovskite–0.1% PCBM devices are shown in Figure 2c.

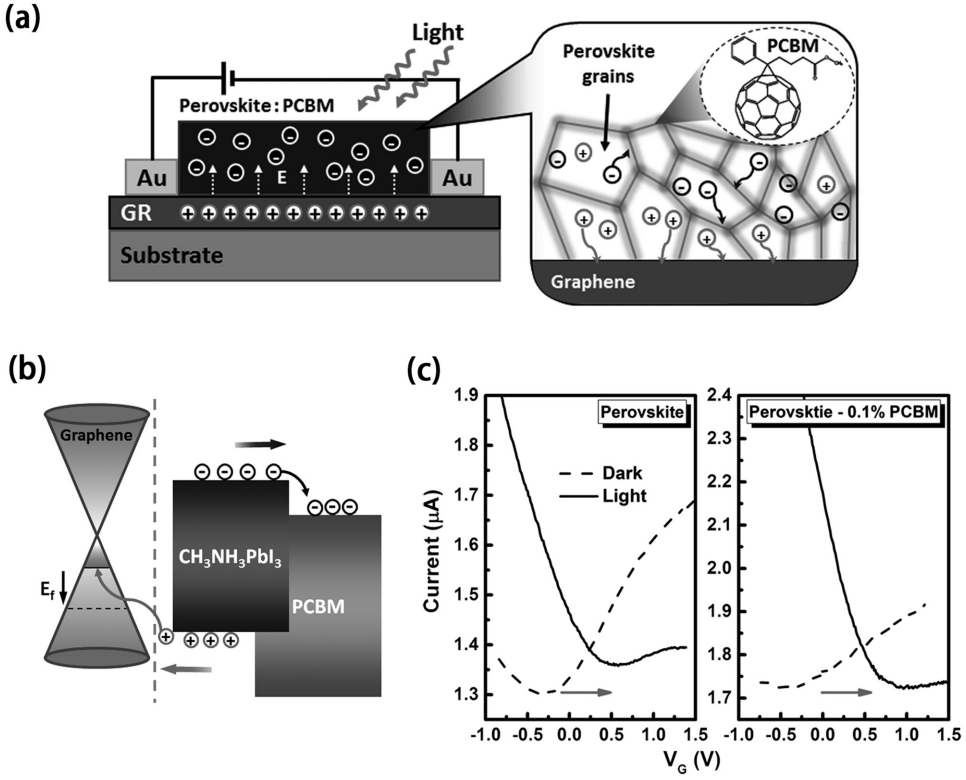

Figure 2. a) A schematic diagram showing the electronic processes occur in the BHJ/graphene photodetector. Previous study[31] has proposed that the PCBM grains are located at the perovskite grain boundaries. The schematic is drawn accordingly, but the actual location of the PCBM grains is not critical in our work. b) The energy level diagram of the PCBM–perovskite/graphene system. c) The source–drain current as a function of the gate voltage for the perovskite-only and the perovskite–0.1% PCBM/GFET devices. The shift of the Dirac point to the positive direction after light irradiation (indicated by arrows) indicates a photoinduced hole doping in graphene.

In these measurements, a PLZT gate underneath the graphene is used so that the position of the E_f with respect to the Dirac point can be measured without applying a large gate voltage.[36] The gate voltage where the minimum current is found represents the voltage needed to move the E_f to the Dirac point.[37] In both samples, the minimum current (Dirac point) is reached at a negative gate voltage prior to light irradiation (dash curves) due to the residual charge on the GFET surface. After the sample is exposed to a white light source (solid curves), the Dirac point shifts to the positive gate voltage direction (indicated by the arrow), indicating that the graphene's E_f moves to a lower energy after light exposure. Hence, optical excitation induces hole doping in graphene. Our result shows that hole transfer is favored at the perovskite–graphene interface even for the perovskite-only device. The addition of PCBM amplifies this bias by trapping electrons in the PCBM domains. As it can be seen from Figure 2c, the shift in the Dirac point is more pronounced for the 0.1% PCBM sample compared to the perovskite-only sample. These results are consistent to the scenario as shown in Figure 2a,b.

After establishing that the holes are preferentially transferred to graphene, the lifetime of trapped electrons within the BHJ layer was evaluated because the responsivity generally increases with the lifetime of the trapped carriers. This is done by measuring the temporal change in the resistance of the graphene channel after the device is excited by a single femtosecond (fs) laser pulse (see the Experimental Section). **Figure 3**a shows the percentage change ($\Delta r/r_0$) of the graphene resistance as a function of time. Note that the resistance decreases after the sample is exposed to light and Δr is negative. The initial change in the channel resistance for $t < 1$ µs is caused by the hole transfer to graphene, which results in an accumulation of negative charges in the sensitizer layer. In Figure 3a, it can be seen that both the signal rise time and the total change in $\Delta r/r_0$ increase with the PCBM concentration. The increase in the overall resistance change indicates that the yield of charge separation is improved with the addition of PCBM. The maximum signal is increased by a factor of ≈4 in the 1% PCBM detector as compared to the perovskite-only detector. Hence, the BHJ allows effective charge separation and reduces the electron–hole recombination in the active layer. On the other hand, the longer signal rise time implies that more time is needed for the hole to transport to graphene. Here, we note that the signal cannot be produced by the charge separation at perovskite–PCBM interfaces alone, but holes also need to transfer to graphene to produce the photogating effect. The slower hole transport can be caused by the disruption of the columnar grain structure in the perovskite–PCBM films (see the SEM images in the Supporting Information), which slows the hole transport along the vertical direction across the BHJ film.

The trapped electrons within the active layer can eventually de-trap and transport to the graphene layer. This electron transfer process, which reduces the net carrier concentration in the sensitizer layer, leads to the decay of the signal. The signal decays with multiple timescales (note that the time axis is in a log-scale), which indicates that a variety of traps with very different de-trapping times are present in the film. For the perovskite-only reference device, majority of the signal decays on the microsecond-timescale. In contrast, after the addition of the PCBM, the lifetime of the trapped carriers increases drastically by ≈4–5 orders of magnitude. For the 1% PCBM sample, some trapped electrons reside in the film up to several seconds after the initial optical excitation. This shows that the PCBM is very effective in trapping the electrons. For samples with long electron lifetime, we wait for the graphene channel to restore its original resistance (the dark resistance) before it is irradiated by another laser pulse. This ensures that all the doped carriers in graphene, which are induced by trapped electrons in PCBM, are removed prior to each measurement. The raw data from some of these repetitive measurements are shown in the Supporting Information. The improved charge separation efficiency and the increase in the electron lifetime are expected to improve the photoresponsivity of the perovskite–PCBM device as compared to the perovskite-only device.

We have also illuminated the 0.1% PCBM device with multiple fs laser pulses to understand how the photoresponse is built up. The result is shown in Figure 3b. In this measurement, the device is excited by a train of 1000 laser pulses (the energy per pulse is same as the one used previously) with two neighboring pulses separated by 0.1 ms. Hence, the sample is under the pulse-laser irradiation for the first 0.1 s. The inset (with a higher time resolution) shows the transient dynamics

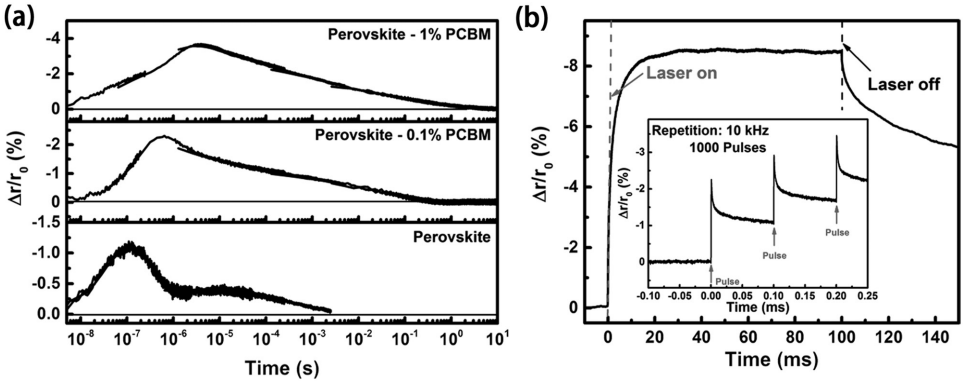

Figure 3. a) The temporal change in the graphene channel resistance after the device is exposed to a single fs laser pulse at $t = 0$. b) The cumulative resistance change in the perovskite–0.1% PCBM device when it is irradiated by a train of 1000 pulses (each pulse is separated by 0.1 ms). The inset is a magnified view showing the photoresponse from the first three pulses.

from the first three laser pulses. Because the lifetime of the trapped electrons is much longer than the temporal separation between two laser pulses, the response from the first pulse cannot be fully recovered before the next pulse arrives. As a result, the response from the pulses accumulates until it saturates after ≈300 pulses (main panel of Figure 3b). The signal saturation behavior can be understood by the increase in the electron–hole recombination rate and the saturation of the electron traps as the carrier concentration becomes too high. Moreover, charge separation builds up an E-field in the sensitizer layer (see Figure 2a) that counteracts further hole injection into the graphene layer. The saturation behavior explains why the photoresponsivity is generally higher when the detector is irradiated by lower intensity light. The results also demonstrate that the response time of the device under continuous light irradiation depends on how fast the device is saturated, rather than the intrinsic charge injection time into graphene. The latter time can be much shorter and is on the order of nanoseconds to few microseconds as shown in Figure 3a.

After elucidating the electronic processes occur in the BHJ–graphene heterostructure, the device performance for samples with different PCBM concentrations is compared. Similar to typical photodetector measurements, a continuous light source with a controllable intensity is used to excite the device. All the devices have a graphene channel length and width of 0.3 and 2 mm, respectively. A source–drain voltage of 1 V is applied across the device and the current across the device is measured. The typical dynamic responses of devices when the light is turned on and off are shown in **Figure 4**a. In order to compare the performance of the three different devices, the percentage change in the source–drain current ($\Delta I_{light}/I_{dark}$) is plotted ($I_{dark}$ is the dark current). When the light is turned on, the percentage change in the current for the 0%, 0.1%, and 1% PCBM devices are ≈32%, ≈43%, and ≈80%, respectively. Clearly, the device with the highest PCBM concentration has the strongest photoresponse. Note that the incident light intensity used for these measurements is relative high, and the devices are highly saturated. Therefore, a relative small difference in the responsivities for devices with different PCBM concentration is observed.

The rising times (the times when 70% of the total response is reached) obtained from Figure 4a for the 0%, 0.1%, and 1% PCBM devices are 2.5, 49, and 92 s, respectively. The longer signal rise time found in the BHJ devices indicates that a longer time is needed to attain the equilibrium carrier concentration within the sensitizer layer. This behavior is expected because as shown in Figure 3a, the de-trapping of electrons from PCBM is an extremely slow process that can last up to a few seconds. The dynamic equilibrium is established when the rate of trapped carrier creation is equal to the rate of trapped carrier de-trapping/annihilation. From Figure 3a, we find that traps with a wide range of de-trapping times exist in sensitizer films. Generally, the equilibrium concentration of trapped carriers increases with the de-trapping time. Hence, under continuous light irradiation, the photoresponse should be originated primarily from the accumulation of electrons in "deep" traps that have the long de-trapping times. These "deep" traps would be larger-sized PCBM aggregates embedded in the perovskite. Because of the band offset at the PCBM–perovskite interface (Figure 2a), these isolated PCBM aggregates act as potential wells for electrons. A sample with a higher PCBM concentration is likely to have more PCBM aggregates, which can account for the slower response of the 1% PCBM sample.

The slow carrier de-trapping can increases the device response time significantly although the trapped carrier creation takes a much shorter time (nanoseconds to microseconds). Similarly, the signal recovery time after the light is turned off are 65 s, 226 s, and 6203 s (time when 70% of the response is recovered) for the 0%, 0.1%, and 1% PCBM devices, respectively. For high PCBM concentration, the longer recovery time is attributed to the slow release of electrons from deep traps in PCBM domains. Therefore, the main trade-off of adding PCBM is the slower device response time.

We note that the signal rising and recovery times observed in Figure 4a are much longer than that observed in Figure 3b. This can be explained by the very different excitation conditions provided by the fs laser and the continuous light source. For the measurement shown in Figure 3b, the sample is excited by a train of fs laser pulses for 0.1 s with a time-averaged incident power of ≈2 mW. In contrast, the continuous light source used for the measurement shown in Figure 4a has an incident power of only 10 μW, but the light exposure time is much longer (500 s). The higher power of the laser source allows the same amount of trapped electrons to be populated in a much shorter period time, which results in the shorter signal rise time.

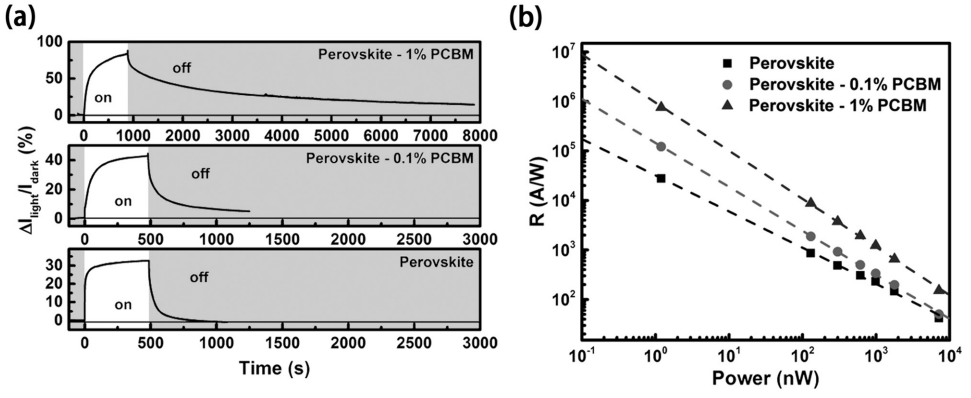

Figure 4. a) The dynamic responses of devices with different PCBM concentrations. The green area represents times when the light source is on. The wavelength of the light source is 500 nm. b) The photoresponsivities as a function of the incident light power on the graphene channel.

Despite the higher power, the total incident energy (laser: 0.2 mJ, continuous light: 5 mJ) is lower for laser irradiation because of the shorter exposure time. Indeed, the total signal response in the 0.1% PCBM sample resulting from continuous light irradiation (≈30% decrease in resistance) is larger than that from laser irradiation (≈8% decrease in resistance). As mentioned above, a long exposure time also biases the filling of traps with longer de-trapping times. The filling of more and deeper electron traps with the continuous light source can account for the longer signal recovery time observed in Figure 4a.

In most of the photodetector measurements, the photoresponsivity can increase with a decrease in the incident light intensity.[10,13,17] As mentioned earlier, a reduced light intensity results in a lower carrier concentration in the sensitizer layer, which generally reduces the electron–hole recombination or other carrier–carrier annihilation processes. The photoresponsivities R for the three devices as a function of incident light power P are shown in Figure 4b, which is calculated using $R = \Delta I/P$. As expected, a higher photoresponsivity can be achieved by a weaker light intensity. For an incident power of 1.2 nW, the photoresponsivity of the pure perovskite device is 3×10^4 A W^{-1}.[17,18] With the addition of PCBM, the photoresponsivity increases to 1×10^5 A W^{-1} for the 0.1% PCBM device and 8×10^5 A W^{-1} for the 1% PCBM device under the same incident power. For the 1% PCBM device, this represents a factor of ≈30 increase in the responsivity compared to the device without PCBM. If we interpolate the curves to lower intensities, the improvement in the responsivity would be even larger.

The enhanced responsivity in devices with PCBM could be attributed to the additional photoconductive gain because of the increased carrier life time demonstrated above. In this nanohybrid photodetectors, the photoconductive gain is mainly determined by the ratio of the carrier life time in the sensitizer (T_{life}) and the carrier transit time in the graphene channel ($T_{transit}$).[10] The T_{life} can be determined from the rising time constants,[10] which are 2.5, 49, and 92 s, respectively, for the 0%, 0.1% and 1% PCBM devices. Assuming the same $T_{transit}$ for the graphene in the three samples, an increase of the photoconductive gain up to a factor of ≈37 is anticipated from the change in the T_{life} from 2.5 to 92 s. This number is pretty close to the ≈27 times increase in the responsivity from the 0% (3×10^4 A W^{-1}) to the 1% PCBM (8×10^5 A W^{-1}) device. Further enhancement of the responsivity can be achieved by reducing the area of the graphene channel.[9,38]

3. Conclusion

In conclusion, we demonstrate that adding electron acceptors into the sensitizer layer of a semiconductor–graphene photodetector can significantly enhance its photoresponsivity. In this particular study, a sensitizer layer consists of a perovskite–PCBM BHJ is used to demonstrate this hypothesis. By using optical spectroscopy and ultrafast time-resolved measurement, it is found that the BHJ–graphene devices have much improved electron–hole separation efficiency and carrier lifetime compared to the pure perovskite–graphene device. These findings correlate well with the device performance. We find that the perovskite with 1% PCBM device has a photoresponsivity of 8×10^5 A W^{-1}, which is about 30 times larger than the photoresponsivity of the perovskite-only device. A setback for the high photoresponsivity is a slow response time due to the increase in the carrier trapping time. The devices used in this study have a relative large channel size (0.3 mm × 2 mm). It is expected that the photoresponsivity could be further improved by using a micrometer-sized GFET device. The use of a BHJ on a GFET can be a general strategy for improving the photoresponsivity of sensitizer/GFET devices for extreme low-light detection.

4. Experimental Section

Sample Preparation: Monolayer graphene on SiO_2/Si or glass substrates was prepared by the standard polymethylmethacrylate (PMMA)-assisted wet transfer method from chemical-vapor deposition (CVD)-grown monolayer graphene on Cu foil purchased from Graphene Supermarket. The PMMA (Sigma-Aldrich, $M_w \approx 996\,000$) was dissolved in chlorobenzene (Macron, 46 mg mL^{-1}) and stirred at 70 °C overnight. Then, a thin PMMA layer was spin-coated on the graphene/Cu foil (3000 rpm, 1 min) and annealed at 120 °C for 15 min. The graphene on the backside of the copper was removed by argon ion sputtering in a vacuum chamber. The Cu foil was etched with an etchant (Transene, UN2582) and rinsed in deionized water, hydrochloric acid, and ammonium hydroxide, consecutively. The graphene layer supported by the PMMA layer was then transferred onto a precleaned substrate (either glass or SiO_2/Si). After the sample is dried and baked under 150 °C for 15 min, the PMMA support layer was removed using hot acetone (80 °C) and rinsed in isopropyl alcohol for three times. The graphene channel was patterned by shadow mask and argon ion sputtering. The metal electrode was deposited in UHV chambers with a shadow mask.

The $CH_3NH_3PbI_3$ precursor solution was prepared by a one-step spin-coating method. The lead iodide (Alfa Aesar, 99.9985%) and methylammonium iodide (Luminescence Technology, 99.5%) in a stoichiometric ratio were dissolved in dimethyl formamide (DMF) (Sigma-Aldrich, 99.8%) with a concentration of 0.75 M. The solution was stirred at 70 °C overnight before spin-coating. For perovskite–PCBM BHJ films, PCBM (Luminescence technology, 99.5%) was mixed into the perovskite solution. In our experiments, three different PCBM weight ratios: 0%, 0.1%, and 1% were selected. PCBM was first dissolved into chlorobenzene solution. The PCBM to perovskite ratio was controlled by mixing the required volume of the PCBM chlorobenzene solution and the $CH_3NH_3PbI_3$ precursor solution. The same volume of chlorobenzene was added into the perovskite solution for preparing the 0% control device. Because of the limited solubility of the PCBM, the resultant solution was only fully miscible for low PCBM concentrations (≤1%). The perovskite–PCBM film was deposited on a preheated graphene substrate (at 80 °C) by spin-coating at 500 rpm for 30 s and then at 3000 rpm for 60 s in a nitrogen glovebox. During the spin-coating, the antisolvent (isopropyl alcohol) was dropped onto the film. Then, the perovskite film was annealed at 70 °C for 20 min, and 100 °C for 10 min to remove the residual solvent.

Film Characterization: The perovskite–PCBM films deposited on the graphene/glass substrate were characterized by various techniques. A field emission scanning electron microscope (FE-SEM, Hitachi-S4800) was used to obtain SEM images. The XRD patterns were recorded by a Bruker D8 Advance X-ray diffractometer with an aluminum sample stage. The UV–vis absorption spectra were collected by a Shimadzu UV-3101PC spectrometer. The photoluminescence spectra were measured in a home-built setup using a standard UV–vis spectrometer.

Ultrafast Measurement: For the ultrafast measurement, devices made on graphene/glass substrate were used. These devices did not have a back gate and a graphene channel size of 1 mm × 1 mm was used. An amplified ytterbium-doped potassium gadolinium tungstate (Yb:KGW) laser system (Light Conversion, PHAROS) was used to seed a

noncollinear optical parametric oscillator (Light Conversion, ORPHEUS-N-2H). The fs laser pulses used have a wavelength centered at 700 nm. The pulse energy and pulse duration are ≈380 nJ and ≈25 fs, respectively. The full-width half maxima beam size at the sample was about 1.1 mm, which covered the whole graphene channel. About half of the laser energy is incident on the sample. During the experiment, the sample was mounted in a high vacuum (10^{-6} Torr) cryostat. The samples, which had different PCBM concentrations (0%, 0.1%, and 1%), were excited by a single or multiple fs laser pulses. The intensity of the pulse was around 20 μJ cm^{-2}. A constant voltage of 1 V was applied across the photodetector and a reference resistor connected in series (Figure S4, Supporting Information). A change in the graphene channel resistance resulted in a change in the potential drop across the reference resistor, which was captured by a 200 MHz oscilloscope. The temporal resolution of our setup was around 50 ns, which was mainly limited by how fast the current could be changed inside the measurement circuit upon the change in the channel resistance. The details of the measurement circuit are discussed in the Supporting Information.

Device Measurement: The optoelectronic properties under the exposure to a continuous light source in visible spectrum was measured using devices made on graphene/SiO_2/Si substrates. The channel length and width were 0.3 and 2 mm respectively. A 500 nm light source was used. A source–drain voltage of 1 V was applied. The source–drain current was measured with an electrochemical workstation (CH Instruments, CHI660D). The light intensity was measured by a Newport optical power meter. Before the measurement, the devices were kept in dark overnight. During the experiment, the devices were kept in dark other than the time when it was irradiated by the light source used in the experiment. The Dirac curve measurements in Figure 2c were obtained by an Agilent Power Device Analyzer (B1505A). To minimize the leakage from the back gate, a GFET device grown on the ferroelectric $Pb_{0.92}La_{0.08}Zr_{0.52}Ti_{0.48}O_3$ (PLZT) back gate were used. The details on the preparation of the PLZT gates and graphene field effect transistors on PLZT gates can be found in ref. [36].

Supporting Information

Supporting Information is available from the Wiley Online Library or from the author.

Acknowledgements

This work was supported by US National Science Foundation grants DMR-1351716, DMR-1337737, and DMR-1508494 and Army Research Office grant W911NF-16-1-0029. The investigation was also supported by the University of Kansas General Research Fund allocation #2151080. Y.H. acknowledges the support from Natural Science Foundation of China (Grant Nos. 61475017, 61377028, 61275175, 61674012, and 61675018) and from National Key Research and Development Program of China (Grant No. 2016YFB0700700).

Conflict of Interest

The authors declare no conflict of interest.

Keywords

bulk heterojunction, GFET, graphene, organometallic hybrid perovskite, photodetectors

Received: July 24, 2017
Revised: September 6, 2017
Published online: October 23, 2017

[1] F. Bonaccorso, Z. Sun, T. Hasan, A. C. Ferrari, *Nat. Photonics* **2010**, *4*, 611.
[2] J. Park, Y. H. Ahn, C. Ruiz-Vargas, *Nano Lett.* **2009**, *9*, 1742.
[3] F. N. Xia, T. Mueller, Y. M. Lin, A. Valdes-Garcia, P. Avouris, *Nat. Nanotechnol.* **2009**, *4*, 839.
[4] Y. J. Yu, Y. Zhao, S. Ryu, L. E. Brus, K. S. Kim, P. Kim, *Nano Lett.* **2009**, *9*, 3430.
[5] E. V. Castro, K. S. Novoselov, S. V. Morozov, N. M. R. Peres, J. M. B. L. Dos Santos, J. Nilsson, F. Guinea, A. K. Geim, A. H. Castro Neto, *Phys. Rev. Lett.* **2007**, *99*, 216802.
[6] W. Chen, S. Chen, D. C. Qi, X. Y. Gao, A. T. S. Wee, *J. Am. Chem. Soc.* **2007**, *129*, 10418.
[7] T. Ohta, A. Bostwick, T. Seyller, K. Horn, E. Rotenberg, *Science* **2006**, *313*, 951.
[8] F. H. L. Koppens, T. Mueller, P. Avouris, A. C. Ferrari, M. S. Vitiello, M. Polini, *Nat. Nanotechnol.* **2014**, *9*, 780.
[9] G. Konstantatos, M. Badioli, L. Gaudreau, J. Osmond, M. Bernechea, F. P. G. de Arquer, F. Gatti, F. H. L. Koppens, *Nat. Nanotechnol.* **2012**, *7*, 363.
[10] M. G. Gong, Q. F. Liu, B. Cook, B. Kattel, T. Wang, W. L. Chan, D. Ewing, M. Casper, A. Stramel, J. Z. Wu, *ACS Nano* **2017**, *11*, 4114.
[11] Z. H. Sun, Z. K. Liu, J. H. Li, G. A. Tai, S. P. Lau, F. Yan, *Adv. Mater.* **2012**, *24*, 5878.
[12] M. Freitag, T. Low, W. J. Zhu, H. G. Yan, F. N. Xia, P. Avouris, *Nat. Commun.* **2013**, *4*, 1951.
[13] W. C. Tan, W. H. Shih, Y. F. Chen, *Adv. Funct. Mater.* **2014**, *24*, 6818.
[14] S. Jang, E. Hwang, Y. Lee, S. Lee, J. H. Cho, *Nano Lett.* **2015**, *15*, 2542.
[15] Q. F. Liu, B. Cook, M. G. Gong, Y. P. Gong, D. Ewing, M. Casper, A. Stramel, J. D. Wu, *ACS Appl. Mater. Interfaces* **2017**, *9*, 12728.
[16] H. Xu, J. X. Wu, Q. L. Feng, N. N. Mao, C. M. Wang, J. Zhang, *Small* **2014**, *10*, 2300.
[17] Y. Lee, J. Kwon, E. Hwang, C.-H. Ra, W. J. Yoo, J.-H. Ahn, J. H. Park, J. H. Cho, *Adv. Mater.* **2015**, *27*, 41.
[18] Y. Wang, Y. Zhang, Y. Lu, W. Xu, H. Mu, C. Chen, H. Qiao, J. Song, S. Li, B. Sun, Y.-B. Cheng, Q. Bao, *Adv. Opt. Mater.* **2015**, *3*, 1389.
[19] M. Spina, M. Lehmann, B. Nafradi, L. Bernard, E. Bonvin, R. Gaal, A. Magrez, L. Forro, E. Horvath, *Small* **2015**, *11*, 4824.
[20] Z. H. Sun, L. Aigouy, Z. Y. Chen, *Nanoscale* **2016**, *8*, 7377.
[21] D. H. Kwak, D. H. Lim, H. S. Ra, P. Ramasamy, J. S. Lee, *RSC Adv.* **2016**, *6*, 65252.
[22] V. Q. Dang, G. S. Han, T. Q. Trung, L. T. Duy, Y. U. Jin, B. U. Hwang, H. S. Jung, N. E. Lee, *Carbon* **2016**, *105*, 353.
[23] C. Xie, F. Yan, *ACS Appl. Mater. Interfaces* **2017**, *9*, 1569.
[24] W. Y. Nie, H. H. Tsai, R. Asadpour, J. C. Blancon, A. J. Neukirch, G. Gupta, J. J. Crochet, M. Chhowalla, S. Tretiak, M. A. Alam, H. L. Wang, A. D. Mohite, *Science* **2015**, *347*, 522.
[25] M. A. Green, A. Ho-Baillie, H. J. Snaith, *Nat. Photonics* **2014**, *8*, 506.
[26] G. Xing, N. Mathews, S. Sun, S. S. Lim, Y. M. Lam, M. Gratzel, S. Mhaisalkar, T. C. Sum, *Science* **2013**, *342*, 344.
[27] J. J. M. Halls, C. A. Walsh, N. C. Greenham, E. A. Marseglia, R. H. Friend, S. C. Moratti, A. B. Holmes, *Nature* **1995**, *376*, 498.
[28] G. Yu, J. Gao, J. C. Hummelen, F. Wudl, A. J. Heeger, *Science* **1995**, *270*, 1789.
[29] C. H. Chiang, C. G. Wu, *Nat. Photonics* **2016**, *10*, 196.
[30] F. Zhang, W. D. Shi, J. S. Luo, N. Pellet, C. Y. Yi, X. Li, X. M. Zhao, T. J. S. Dennis, X. G. Li, S. R. Wang, Y. Xiao, S. M. Zakeeruddin, D. Q. Bi, M. Gratzel, *Adv. Mater.* **2017**, *29*, 1606806.
[31] J. Xu, A. Buin, A. H. Ip, W. Li, O. Voznyy, R. Comin, M. J. Yuan, S. Jeon, Z. J. Ning, J. J. McDowell, P. Kanjanaboos, J. P. Sun, X. Z. Lan, L. N. Quan, D. H. Kim, I. G. Hill, P. Maksymovych, E. H. Sargent, *Nat. Commun.* **2015**, *6*, 7081.

[32] G. A. Elbaz, D. B. Straus, O. E. Semonin, T. D. Hull, D. W. Paley, P. Kim, J. S. Owen, C. R. Kagan, X. Roy, *Nano Lett.* **2017**, *17*, 1727.
[33] N. J. Jeon, J. H. Noh, Y. C. Kim, W. S. Yang, S. Ryu, S. Il Seol, *Nat. Mater.* **2014**, *13*, 897.
[34] T. Baikie, Y. N. Fang, J. M. Kadro, M. Schreyer, F. X. Wei, S. G. Mhaisalkar, M. Graetzel, T. J. White, *J. Mater. Chem. A* **2013**, *1*, 5628.
[35] S. Falke, P. Eravuchira, A. Materny, C. Lienau, *J. Raman Spectrosc.* **2011**, *42*, 1897.
[36] C. R. Ma, Y. P. Gong, R. T. Lu, E. Brown, B. H. Ma, J. Li, J. Wu, *Nanoscale* **2015**, *7*, 18489.
[37] J. B. Oostinga, H. B. Heersche, X. L. Liu, A. F. Morpurgo, L. M. K. Vandersypen, *Nat. Mater.* **2008**, *7*, 151.
[38] R. T. Lu, J. W. Liu, H. F. Luo, V. Chikan, J. Z. Wu, *Sci. Rep.* **2016**, *6*, 19161.